buildings

MDPI

Article

Performance and Mesostructural Characterization of Asphalt Mixtures with Molybdenum Tailings as Mineral Filler

Jingyuan Zhang [1,2], Bokai Wang [3], Lei Liu [3], Bing An [3], Jinlong Liu [1], Junqi Lin [1,*] and Hongshuai Gao [3,*]

[1] Key Laboratory of Earthquake Engineering and Engineering Vibration, Institute of Engineering Mechanics, China Earthquake Administration, Harbin 150080, China; zhangjingyuan2022@126.com (J.Z.); liujinlong@iem.ac.cn (J.L.)
[2] Heilongjiang Provincial Transportation Planning and Design Institute Group Co., Ltd., Harbin 150080, China
[3] School of Civil Engineering, Heilongjiang University, Harbin 150080, China; wangbokai101@163.com (B.W.); liuleihdjg@126.com (L.L.); anbing1226@163.com (B.A.)
* Correspondence: linjunqi1964@163.com (J.L.); hongshuai.gao@hlju.edu.cn (H.G.)

Abstract

This study evaluates molybdenum tailings (MT) as a substitute for limestone filler (LF) in asphalt mixtures. MT replaced LF on an equal volume basis. The replacement ratio ranged from 0% to 100%. The study conducted wheel tracking tests, three-point bending tests, immersion tests, and indirect tensile splitting tests. A representative MT100 mixture was selected for industrial CT scanning with VGStudio Max. The maximum entropy method was used for image segmentation. The method quantified aggregate, mastic, and air void phases. The results show that MT improved rutting resistance. Dynamic stability increased from 1071 passes/mm at 0% replacement to 1548 passes/mm at 100% replacement. The flexural stiffness modulus increased by 73.60% relative to the control at 100% MT replacement. Residual stability reached 86.92% at 100% replacement. CT observations of the 100% MT specimens showed an asphalt mastic phase surrounding the aggregate skeleton and dispersed air voids. The observed vertical nonuniformity was interpreted as a compaction-related structural feature associated with Marshall mold boundary effects. In conclusion, MT shows potential as an alternative mineral filler for improving asphalt mixture performance.

Keywords: molybdenum tailings; asphalt mixture; pavement performance; industrial CT

Check for updates

Academic Editor: Antonio Caggiano

Received: 25 September 2026
Revised: 25 October 2026
Accepted: 26 October 2026
Published: 2 November 2026

Copyright: © 2026 by the authors. Licensee MDPI, Basel, Switzerland. This article is an open access article distributed under the terms and conditions of the Creative Commons Attribution (CC BY) license.

1. Introduction

Mining activities support economic development, but they also generate large volumes of tailings and lead to long-term environmental and safety burdens [1–3]. Tailings storage usually requires extensive land occupation and continuous management. As containment structures age, they may pose risks to surrounding ecosystems and infrastructure [4]. Meanwhile, many tailings contain mineral phases that retain mechanical stability after beneficiation. This feature allows tailings to be regarded as a secondary resource rather than as final waste [5,6]. Tailings reuse can reduce the demand for primary mineral materials and help relieve pressures associated with waste storage and risk control.

In recent years, the utilization of tailings, particularly in construction materials, has advanced rapidly. This field, characterized by high material consumption and strong engineering adaptability, facilitates the large-scale utilization of solid wastes [7,8]. Numerous studies have explored the use of steel slag, fly ash, and various metal tailings as aggregates or fillers in cement-based and asphalt-based systems. Under suitable conditions, these materials can enhance stiffness, strength, or deformation resistance while reducing the

consumption of natural resources [9–11]. These improvements are primarily attributed to optimized particle gradation, densified packing, and stronger mechanical interlock from higher surface roughness [12–14]. Previous research [14] focused on the rheological performance and environmental aspects of MT asphalt mastic. In contrast, the present study investigates the pavement performance of AC-13 asphalt mixtures with different MT replacement levels and characterizes the three-phase spatial distribution and mesostructural nonuniformity of the 100% MT mixture using industrial CT. In addition, the chemical composition of certain wastes can modify the structure of cementitious matrices or asphalt mastic. However, the performance benefits of tailings are not universal and are often highly sensitive to material properties and processing conditions [15]. Due to inherent variations in mineral composition, particle morphology, surface activity, and adsorption behavior, different tailings can significantly alter the viscoelastic response of asphalt mastic and the adhesion at the interface, thereby affecting moisture damage susceptibility, cracking resistance, and long-term durability [16–19]. Moisture resistance, durability, and interface stability remain key bottlenecks for engineering applications [20–24], with test outcomes fluctuating with processing parameters and mix design. Within this context, research on molybdenum tailings as a filler in asphalt mixtures remains limited, with a notable scarcity of evidence from comprehensive performance validation and mesostructural characterization. Therefore, this study aims to evaluate the pavement performance of asphalt mixtures with MT as a mineral filler substitute and characterize the mesostructure of representative 100% MT specimens using CT analysis.

Because of high construction efficiency and ease of maintenance, asphalt pavement remains the most widely used pavement structure in modern road networks [25,26]. Dense graded asphalt mixtures rely on a mineral aggregate skeleton to carry the primary load. They also rely on an asphalt mastic rich in binder to provide bonding and filling between aggregates [27–29]. Mineral filler plays an important role in this system. It participates in the formation of the mastic microstructure. It also changes the viscoelastic properties of the mastic through filling and adsorption. These effects influence deformation and damage evolution of the mixture at different service temperatures [30,31]. The particle size distribution and surface characteristics of the filler affect the viscosity and stiffness of the binder. They further affect high temperature flow stability and rutting resistance [32,33]. In addition, filler regulates the adhesion state at the binder aggregate interface and its sensitivity to moisture. These changes influence moisture damage and durability performance [34–38]. For dense graded mixtures, the interaction between filler and mastic also affects skeleton quality and air void structure. This influence is reflected in pavement performance indices such as deformation resistance, cracking resistance, and water stability [39–42]. Limestone filler is widely used, but its extraction and grinding require substantial energy and increase resource pressure [43]. This situation makes waste-derived fillers a promising alternative. The screening and validation of alternative fillers should cover rutting resistance, cracking resistance, and water stability. The process should also meet requirements for engineering stability and feasibility [44]. In this context, molybdenum tailings represent a metal tailings type with large reserves and high stockpiling pressure. Their performance and structural roles as a filler substitute in asphalt mixtures still need further verification.

This study examines whether MT can fully replace LF in asphalt mixtures on an equal volume basis. The work began by comparing the basic properties and micro morphology of MT and LF to identify characteristics that might affect asphalt mastication and interface behavior. A set of performance tests was then carried out. Rutting resistance was measured with a wheel tracking test. A three-point bending test evaluated intermediate-temperature flexural performance at 15 °C. Resistance to splitting was assessed via an indirect tensile splitting test. Moisture stability was determined using the immersion Marshall method.

To understand the internal structure, representative samples were scanned with industrial CT and reconstructed in three dimensions. The images were segmented to distinguish the aggregate, mastic, and air void phases. This allowed the mesoscale uniformity along the sample height to be quantified. The CT analysis provided descriptive information on the internal phase distribution of the 100% MT mixture, complementing the macroscopic performance evaluation. In summary, this research provides experimental evidence on the performance and underlying structure of asphalt mixtures using MT as a sustainable filler replacement.

2. Experimental Details

2.1. Raw Materials

2.1.1. Asphalt Binder

This study used a base asphalt binder produced by Liaoning Panjin Petrochemical Co., Ltd. (Panjin, Liaoning Province, China). The penetration grade was 90. Its basic properties are listed in Table 1. The test results show that all indices meet the relevant specification requirements. The binder was suitable for asphalt mixture preparation and performance testing in this study.

Table 1. Basic properties of 90# base asphalt.

Asphalt	Properties	Unit	Test Values	Specification Requirements	Test Method
90#	Penetration @ 25 °C	0.1 mm	94.5	80–100	T0604
	Ductility @ 10 °C	cm	52	≥40	T0605
	Softening point	°C	48.7	≥45	T0606
	Viscosity @ 60 °C	Pa.s	205	≥160	T0620
	Density	g/cm^3	1.03	—	T0603
	Flash point	°C	257	≥245	T0611

2.1.2. Aggregates

Aggregates used in this study were supplied by Harbin Zhongpeng Building Materials Co., Ltd., Harbin, China. Basalt was used as the coarse aggregate, and limestone was used as the fine aggregate. Before mixture preparation, the aggregates were dried and sieved to the target size ranges. The basic properties of the aggregates were tested using the standard methods listed in Table 2. All results met the relevant specification requirements.

Table 2. Basic properties of aggregates.

Types	Properties	Unit	Test Values	Specification Requirements	Test Method
Coarse aggregates/Fine aggregates	Crush value	%	19.8/-	≤26/≤10	T0316/T0350
	Los Angeles wear loss	%	18.3/-	≤28/≤30	T0317
	Water absorption	%	0.21/0.35	≤2.0/≤1.0	T0305/T0330
	Apparent density	g/cm^3	2.70/2.768	≥2.6/≥2.5	T0304/T0328
	Bulk density	g/cm^3	1.41/1.29	—/—	T0309/T0331
	Mud content	%	0.46/0.16	≤2.0/≤3.0	T0310/T0333

2.1.3. Fillers

LF was used as the reference filler. It was produced by Boli County Longxin Mineral Powder Manufacturing Co., Ltd. (Boli, China). MT were supplied by Yichun Luming Mining Co., Ltd., Tieli, Yichun, China. The MT was dried, ground, and sieved through

a 0.075 mm sieve before use. MT replaced LF on a volume basis. The replacement ratios were set to 0%, 25%, 50%, 75%, and 100%. The main chemical compositions of LF and MT are presented in Table 3, while their particle size distribution parameters, theoretical specific surface areas, and hydrophilic coefficients are summarized in Table 4. The chemical compositions of LF and MT were determined using X-ray fluorescence (XRF) spectroscopy. The results were expressed as oxide mass fractions (wt.%) and normalized to 100% based on the sum of the reported compositional categories. All test results met the relevant specification requirements. The microstructure of LF and MT is shown in Figure 1.

Table 3. XRF-determined chemical composition of LF and MT (wt.%).

Types	Chemical Composition (wt.%)						
	CaO	**SiO_2**	**Fe_2O_3**	**MnO**	**Al_2O_3**	**K_2O**	**Others**
LF	95.687	3.338	0.734	0.187	/	/	0.054
MT	3.362	71.842	1.853	0.047	11.472	7.32	4.104

Table 4. Physical characteristics of LF and MT.

Properties	Unit	LF	MT
D10	μm	2.554	6.271
D50	μm	26.236	72.878
D90	μm	128.467	164.238
Theoretical specific surface area	m^2/kg	1008	460.3
Hydrophilic coefficient	—	0.72	0.84

Although MT was sieved through a 0.075 mm sieve before use, the measured particle size distribution showed that some particles had equivalent diameters greater than 75 μm, which may be attributed to particle agglomeration during sample handling and measurement.

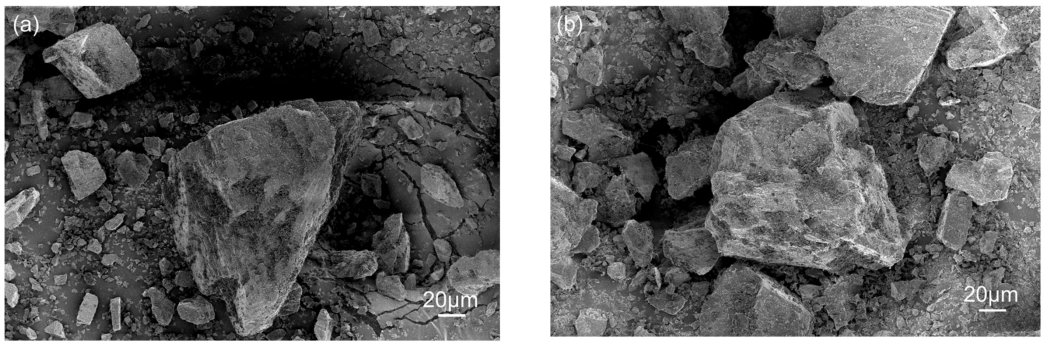


Figure 1. Scanning electron microscopy (SEM) images of the fillers: (**a**) LF; (**b**) MT.

2.2. Mix Design

A dense-graded AC-13 asphalt mixture was selected as the target mixture in this study, and its gradation curve is shown in Figure 2. MT was used to replace LF at volume replacement levels of 0%, 25%, 50%, 75%, and 100%. The apparent densities of LF and MT were 2.74 and 2.64 g/cm^3, respectively. To maintain a constant total filler volume across the mixtures, equal-volume replacement was adopted, and the masses of LF and MT at each replacement level were determined by density conversion.

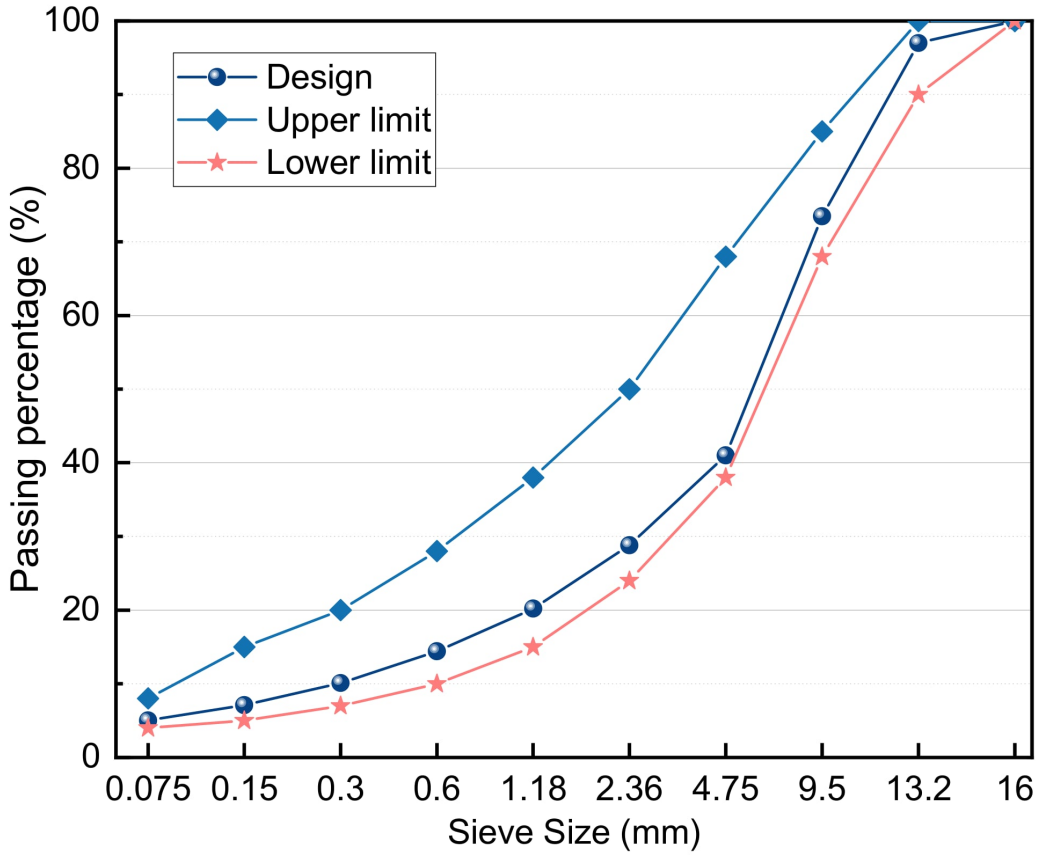


Figure 2. Gradation curves.

Based on the target gradation, coarse aggregate, fine aggregate, and mineral filler accounted for approximately 59%, 36%, and 5% of the total volume of mineral aggregates, respectively. In the reference mixture, the nominal mass proportions of coarse aggregate, fine aggregate, mineral filler, and asphalt binder were 56.17%, 34.27%, 4.76%, and 4.80%, respectively, by total mixture mass. The quantities of LF and MT were adjusted according to the specified volume replacement ratios.

The design asphalt content of 4.8% was determined using the Marshall mix design method and was maintained across all five MT replacement levels to evaluate the effect of filler substitution under a fixed binder-content condition.

2.3. Preparation Process

The specimen preparation procedure is illustrated in Figure 3.

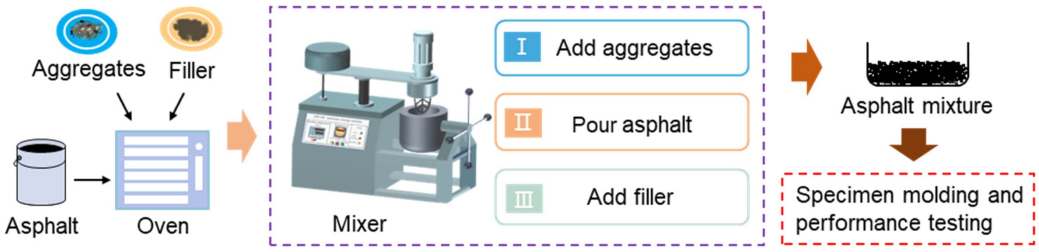


Figure 3. Experimental procedure for asphalt mixture preparation.

(I) The coarse and fine aggregates were dried in an oven to constant mass and sieved according to the target gradation. The filler was dried to remove moisture before use.
(II) The coarse and fine aggregates were weighed according to the target proportions and preblended in a metal tray until uniform.
(III) The actual mixing and compaction temperatures were 146 °C and 131 °C, respectively. The aggregates were preheated in an oven to approximately 15 °C above the mixing temperature. The filler and the 90-penetration grade asphalt binder were heated in parallel and maintained at the required temperature before mixing.
(IV) The preheated aggregates were placed into a mechanical mixer and dry-mixed for about 30 s to achieve uniformity.
(V) The hot binder was added and mixed for 1.5 min.
(VI) Mixing was paused and the preheated filler was added. Mixing then continued for 1.5 min until the mixture was uniformly coated and a continuous binder film formed.
(VII) After mixing, the hot mixture was placed into the corresponding molds and compacted at 131 °C. Marshall specimens were compacted using a standard Marshall impact compactor with a hammer drop height of 457 mm and 75 blows on each face. Slab specimens for wheel tracking tests were compacted using a wheel-rolling compactor.

2.4. Test Method

The error bars in Figures 4–7 illustrate the deviations of individual specimen measurements from their corresponding group means.The descriptive statistics, one-way ANOVA results, and specimen-level three-point bending test data are provided in Supplementary Tables S1–S3, respectively.

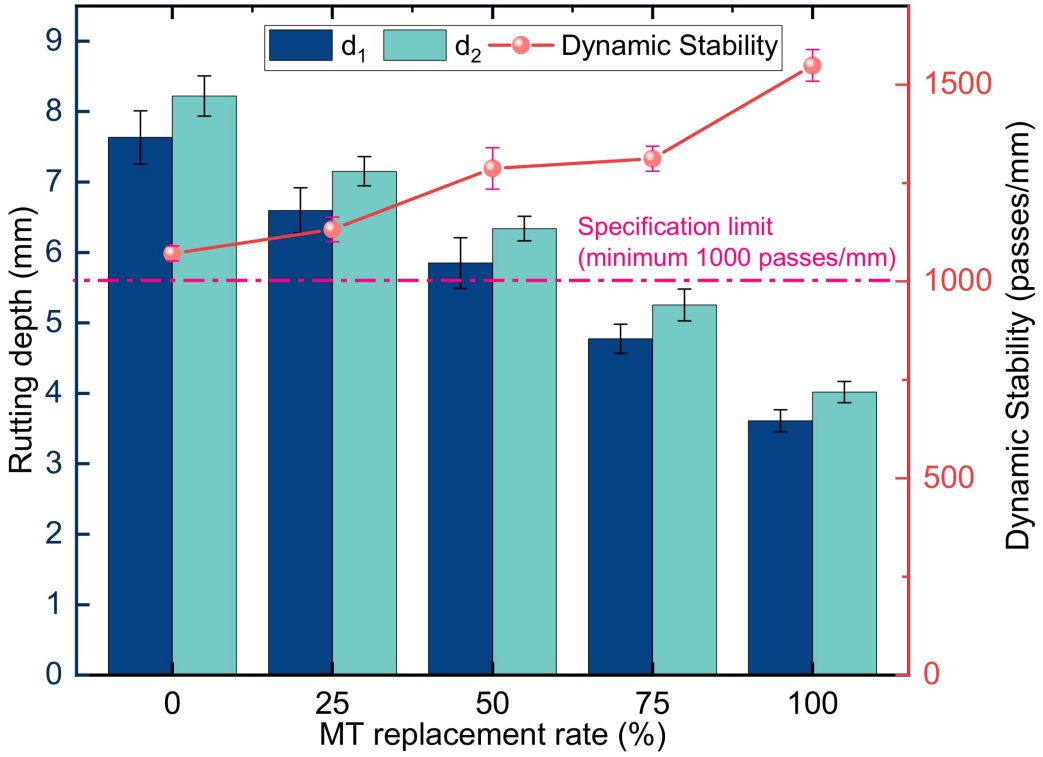


Figure 4. High-temperature rutting performance of asphalt mixtures with different MT replacement rates.

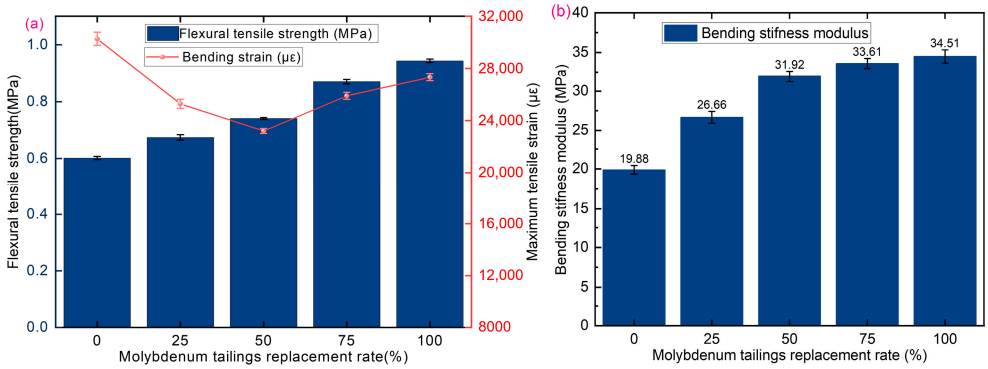


Figure 5. Flexural properties of asphalt mixtures with different MT replacement rates: (**a**) Flexural tensile strength and maximum tensile strain; (**b**) Bending stiffness modulus.

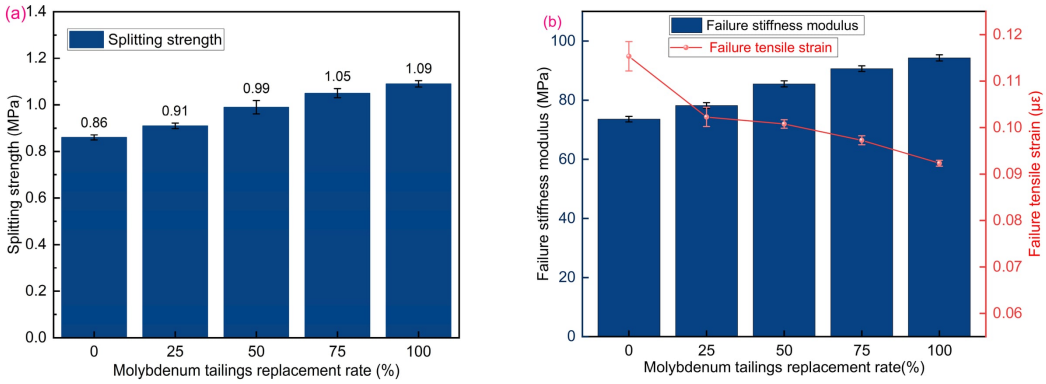


Figure 6. Splitting performance of asphalt mixtures with different MT replacement rates: (**a**) Splitting strength; (**b**) Failure stiffness modulus and failure tensile strain.

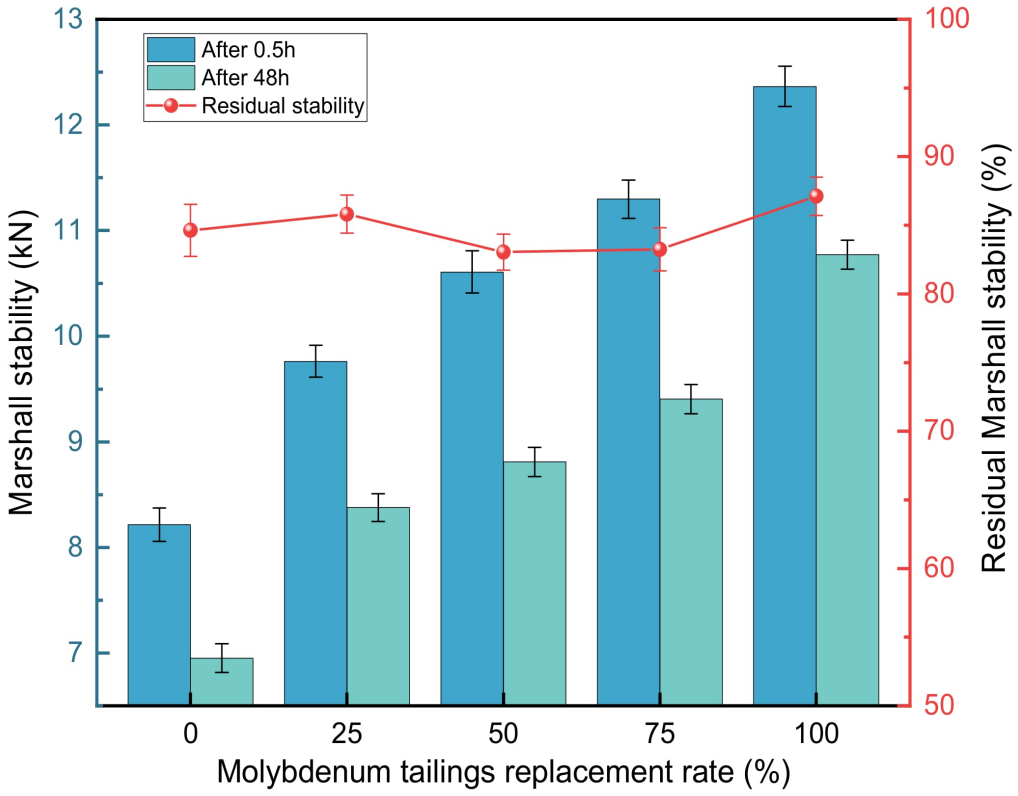


Figure 7. Water stability performance of asphalt mixtures with different MT replacement rates.

2.4.1. Wheel Tracking Test

A wheel tracking test was conducted using an automatic wheel tracking device (model HYCZ-5) to evaluate the high-temperature deformation resistance of the mixtures. The test procedure followed JTG E20-2011 T0719 [45]. Slab specimens with dimensions of 300 mm × 300 mm × 50 mm were prepared using a slab compactor. Before testing, specimens were conditioned at 60 °C for 6 h. Three replicate specimens were prepared for each mixture. During the test, the wheel pressure was 0.7 MPa, and the reciprocating speed was 42 passes/min. The dynamic stability was calculated using Equation (1).

$$DS = \frac{(t_2 - t_1) \times N}{d_2 - d_1} \quad (1)$$

In the formula, DS is the dynamic stability of the asphalt mixture (passes/mm); d_1 is the deformation (mm) at t_1 = 45 min; and d_2 is the deformation (mm) at t_2 = 60 min.

N is the reciprocating wheel passing rate, which was 42 passes/min.

2.4.2. Bending Test

A bending performance test was conducted using a universal testing machine (model WDW-100). The test procedure followed JTG E20-2011 T0715 [45]. Prismatic specimens with dimensions of 250 mm × 30 mm × 35 mm were prepared. Before testing, the specimens were conditioned at 15 °C until thermal equilibrium was reached. A three-point bending configuration was then used. Loading was applied at the midspan at a rate of 50 mm/min until failure. Three replicate specimens were tested for each mixture. The flexural tensile strength at failure (R_B), maximum tensile strain at the bottom fiber at failure (ε_B), and flexural stiffness modulus (S_B) were calculated separately for each specimen, and the corresponding group means were then determined. The dimensionless tensile strain calculated using Equation (3) was multiplied by 10^6 for reporting in microstrain (με), while the dimensionless strain was used to calculate S_B in Equation (4). The calculation formulas are given in Equations (2)–(4).

$$R_B = \frac{3 \times L \times P_B}{2 \times b \times h^2} \quad (2)$$

$$\varepsilon_B = \frac{6 \times h \times d}{L^2} \quad (3)$$

$$S_B = \frac{R_B}{\varepsilon_B} \quad (4)$$

In the formula, R_B is the flexural tensile strength (MPa); L is the span length (mm); P_B is the maximum load (N); b is the specimen width at the midspan section (mm); h is the specimen height at the midspan section (mm); ε_B is the maximum tensile strain (dimensionless in Equations (3) and (4), and converted to με for reporting); d is the midspan deflection (mm); and S_B is the flexural stiffness modulus (MPa).

2.4.3. Indirect Tensile Splitting Test

An indirect tensile splitting test was conducted using a universal testing machine (model WDW-100). The test procedure followed JTG E20-2011 [45]. Before testing, the specimens were conditioned at the test temperature until thermal equilibrium was reached. The test was carried out at 15 °C with a loading rate of 50 mm/min. Three replicate specimens were prepared for each mixture, and the average value was taken as the test result. The maximum load at failure and the corresponding diametral deformation were recorded. The splitting tensile strength, failure tensile strain, and stiffness modulus were calculated using Equations (5)–(7).

$$R_T = 0.006287 P_T / h \quad (5)$$

$$\varepsilon_T = X_T \times (0.0307 + 0.0936\mu)/(1.35 + 5\mu) \quad (6)$$

$$S_T = P_T \times (0.27 + 0.1\mu)/(h \times X_T) \quad (7)$$

In the formula, R_T is the indirect tensile strength (MPa); ε_T is the tensile strain at failure; S_T is the stiffness modulus at failure (MPa); P_T is the maximum applied load (N); h is the specimen height (mm); μ is Poisson's ratio; and X_T is the horizontal deformation (mm).

2.4.4. Water Stability Test

An immersion Marshall test was conducted using a Marshall stability tester (model SYD-0709) to evaluate the water stability of the mixtures. The test procedure followed JTG E20-2011 T0709 [45]. Marshall specimens were divided into two groups and immersed in a water bath at 60 °C for 0.5 h and 48 h, respectively. After immersion, the Marshall stability of the specimens was measured. For each MT replacement level, four independent specimens were tested under each immersion condition (0.5 h and 48 h), and the mean Marshall stability was calculated separately for each conditioning group. The evaluation index was the residual stability, which was calculated using Equation (8).

$$MS_0 = \frac{MS_1}{MS} \times 100\% \quad (8)$$

In the formula, MS_0 is the residual stability of the specimen in water (%); MS_1 is the Marshall stability of the specimen after immersion in water at 60 °C for 48 h (kN); and MS is the Marshall stability of the specimen after immersion in water at 60 °C for 0.5 h (kN).

2.4.5. Industrial CT Scanning and Image Processing

An industrial X-ray computed tomography (CT) system (model RMCT-4000) was used to characterize the internal mesostructure of the asphalt mixtures. Three standard Marshall specimens with 100% MT replacement were scanned at an X-ray tube voltage of 240 kV. The spatial sampling interval of the reconstructed CT data was approximately 90 μm. X-ray projection data were collected from multiple angles and reconstructed into tomographic slices and three-dimensional volumetric data. The reconstructed images were processed and visualized using VGStudio Max software (version 2024.3). The region of interest (ROI) was restricted to the interior of each cylindrical specimen, and a specimen mask was applied to exclude the surrounding background air from phase identification.

3. Results and Discussion

3.1. High-Temperature Rutting Performance

The wheel tracking results in Figure 4 reflect the high-temperature rutting resistance of mixtures with different MT replacement levels. When the MT replacement was 0%, 25%, 50%, 75%, and 100%, the dynamic stability values were 1071, 1132, 1287, 1312, and 1548 passes/mm, respectively. The dynamic stability increased with increasing MT replacement, and all values exceeded the specification limit of 1000 passes/mm. The incremental rut depth, $d_2 - d_1$,was 0.589 mm, 0.557 mm, 0.490 mm, 0.480 mm, and 0.407 mm, respectively. It decreased in a nonlinear manner as the MT replacement increased. These results indicate that rutting accumulation was suppressed at high temperature and the rutting resistance of the mixtures was improved. The equal-volume replacement ensured the same filler volume across mixtures. Therefore, the performance differences mainly originated from filler properties and the resulting changes in mastic behavior and interfacial effects [46]. Compared with LF, MT particles had more angular outlines and a rougher surface. MT also showed a generally coarser particle size distribution. These features made MT act more like a very fine aggregate in the mixture. They can enhance internal friction and mechanical

interlock in the mastic-rich zones. As a result, relative slip between aggregates was reduced and mastic flow under repeated high-temperature loading was restrained [13,47]. This mechanism agrees with the measured filler morphology and particle size results. It explains the increase in dynamic stability and the decrease in incremental rut depth with increasing MT replacement.

3.2. Flexural Performance

Figure 5 presents the flexural test results of mixtures with different MT replacement ratios. As the MT replacement increased, both the flexural tensile strength (R_B) and the flexural stiffness modulus (S_B) showed an overall nonlinear increase, indicating improved flexural load-bearing capacity and deformation resistance. The maximum tensile strain at failure (ε_B) first decreased and then increased, with a minimum mean value of approximately 23,205 με at 50% MT replacement. Compared with the control mixture, S_B increased by 34.14%, 60.54%, 69.05%, and 73.60% at MT replacement levels of 25%, 50%, 75%, and 100%, respectively.

In flexural evaluation, R_B represents the flexural tensile strength at failure, S_B reflects resistance to flexural deformation, and ε_B characterizes the deformation capacity at failure. MT replacement increased R_B and S_B, whereas ε_B showed a nonmonotonic variation, indicating differences in deformation capacity among the mixtures. Overall, the results indicate improved intermediate-temperature flexural load-bearing capacity and stiffness at 15 °C. From the microstructural perspective, MT particles exhibit relatively high rigidity, angular shapes, and rough surfaces. These features can enhance mechanical interlock and interfacial friction within the asphalt mastic, improve load transfer, and restrain local interfacial slip. As a result, the risk of early crack initiation under bending is reduced, which is consistent with the observed increases in R_B and S_B [13,46,47].

3.3. Indirect Tensile Splitting Performance

Figure 6 shows the indirect tensile splitting indices of mixtures with different MT replacement ratios, including splitting tensile strength, tensile strain at failure, and stiffness modulus at failure. As the MT replacement increased from 0% to 100%, the splitting tensile strength increased from 0.85696 MPa to 1.08860 MPa, indicating enhanced load-bearing capacity under splitting. Compared with the control mixture, the splitting strength increased by about 5.6%, 15.4%, 22.2%, and 27.0% at replacement ratios of 25%, 50%, 75%, and 100%, respectively. The stiffness modulus at failure also increased with increasing MT replacement, which indicates improved resistance to deformation. In contrast, the tensile strain at failure gradually decreased as the replacement ratio increased, indicating a potential trade-off between stiffness and deformation capacity. These results demonstrate improvements in splitting strength and stiffness, while their implications for overall cracking resistance require further consideration. Overall, MT replacement of LF effectively improved the splitting tensile strength and the stiffness modulus at failure. The splitting response is governed by the cohesion of the asphalt mastic and the adhesion at the asphalt–aggregate interface. MT particles show angular shapes and rough surfaces, which can enhance interfacial adhesion and mechanical interlock. These effects increase splitting resistance and improve the overall deformation resistance of the mixture [13,48].

3.4. Water Stability

Figure 7 presents the immersion Marshall results of mixtures with different MT replacement ratios. As the MT replacement increased from 0% to 100%, the Marshall stability values under both immersion durations showed an overall increasing trend. This result indicates that the load-bearing capacity and softening resistance after water exposure were

enhanced by MT replacement. Compared with the stability after 0.5 h immersion, the stability after 48 h immersion was generally lower, suggesting that prolonged immersion may weaken the binder system and interfacial adhesion. The residual stability showed only small fluctuations, decreasing slightly at intermediate replacement levels before increasing at higher replacement levels. Therefore, the observed increases in absolute Marshall stability indicate improved load-bearing capacity under the investigated immersion conditions, but do not necessarily demonstrate a substantial reduction in moisture susceptibility. All mixtures had residual stability values higher than the specification requirement of 80%, indicating that the water stability met the engineering requirement at all replacement levels. Water stability is mainly governed by the cohesion of the asphalt mastic and the adhesion at the asphalt–aggregate interface, as well as the sensitivity to moisture damage [49]. MT particles are angular and have rough surfaces, which can enhance mechanical interlock between the mastic and mineral materials and increase interfacial shear resistance. These effects may contribute to the higher Marshall stability observed after water immersion. In addition, MT replacement may modify the structuring effect of filler on the mastic. This change can help the mastic retain higher strength and stability after immersion. This behavior is consistent with the simultaneous increase in Marshall stability after 0.5 h and 48 h immersion and the consistently high level of residual stability.

The immersion Marshall test was selected as a practical method to compare the water stability of asphalt mixtures with different MT replacement levels based on their Marshall stability retention after water immersion. However, this test does not directly evaluate moisture damage under freeze–thaw conditions, for which the freeze–thaw splitting strength ratio test (AASHTO T283/JTG E20 T0729) provides a more targeted assessment, particularly regarding asphalt–aggregate adhesion deterioration and moisture-induced stripping.

3.5. Industrial CT Scanning

The reconstructed CT images were processed using grayscale-based segmentation methods to identify the constituent phases of the asphalt mixtures [50]. The maximum entropy method was used for initial binary segmentation to distinguish aggregates from the remaining material regions [50]. For three-phase classification, a multi-threshold Otsu method was subsequently applied to the original CT grayscale data, automatically determining two segmentation thresholds to distinguish aggregates, asphalt mortar, and air voids. The three phase fractions were calculated within the same cross-sectional region of interest, with their sum equal to 100% for each analyzed cross-section. Figure 8 illustrates the CT image reconstruction, binary segmentation, and three-dimensional visualization of the material phases.

The height-dependent phase distributions varied among the three specimens. In particular, Specimen 1 exhibited a marked increase in asphalt mortar content near one end, as shown in Figure 9d. The height-dependent distribution of aggregate content is presented in Figure 10d, whereas Figure 11d shows a pronounced reduction in air-void content in the middle region of Specimen 3. These specimen-specific variations indicate that the three specimens did not exhibit an identical vertical distribution pattern.

Fine aggregate particles distinguishable from the surrounding asphalt mortar at the CT sampling scale were included in the aggregate phase rather than treated as a separate material phase. Particles below the effective imaging resolution could not be individually resolved.

The apparent continuity of the mastic and aggregate phases and the dispersion of air voids were interpreted qualitatively at the available CT sampling scale, without quantitative connectivity analysis. In addition, the CT-derived air-void contents were not independently validated against experimentally measured air-void contents.

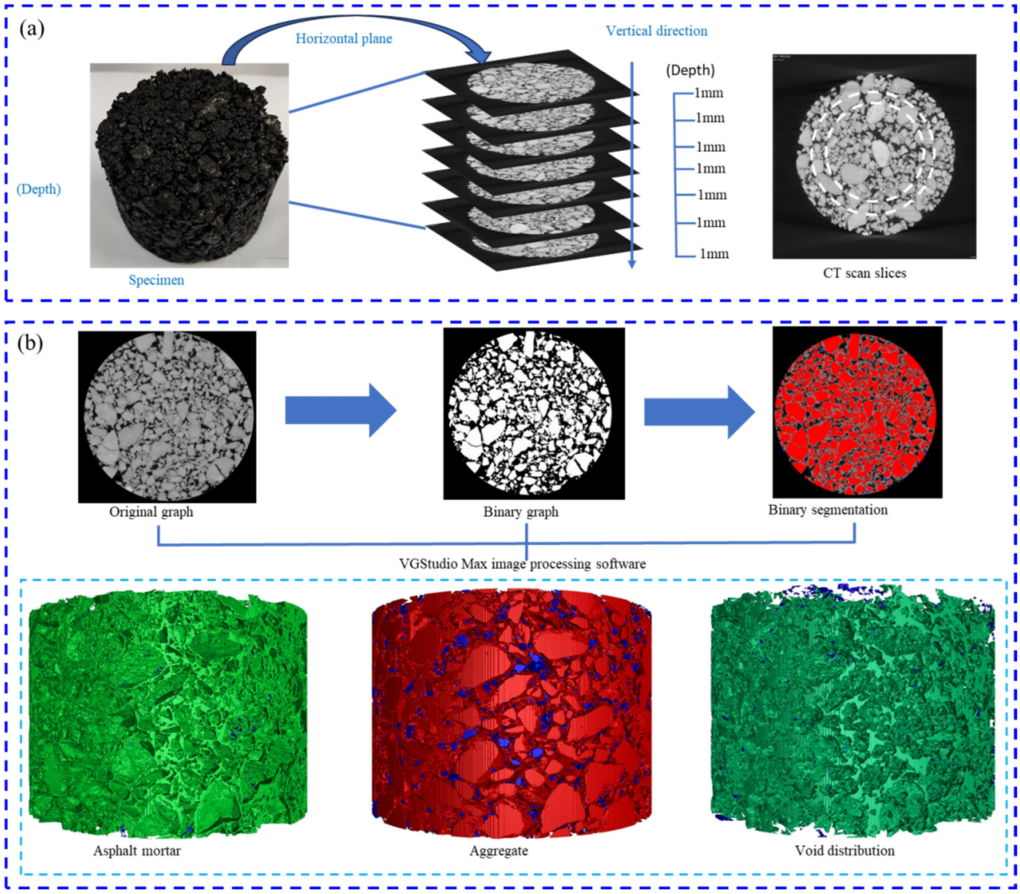


Figure 8. CT image processing and material-phase visualization: (**a**) CT slice reconstruction; (**b**) binary segmentation and three-dimensional visualization of asphalt mastic, aggregates, and air voids.

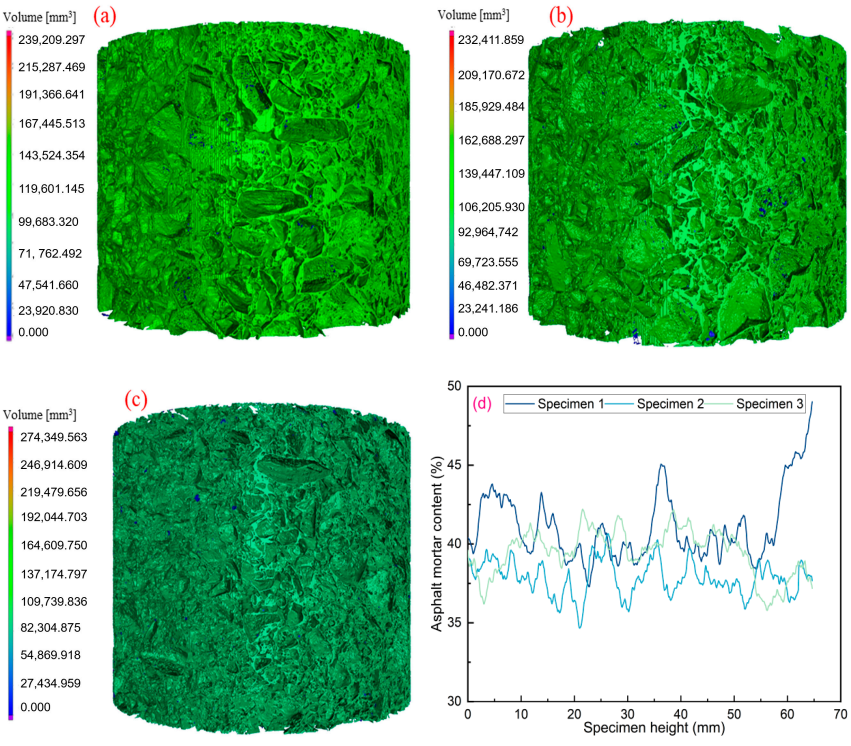


Figure 9. The distributions of asphalt mortar in mixture: (**a**) Specimen 1, (**b**) Specimen 2, (**c**) Specimen 3, and (**d**) Mortar content.

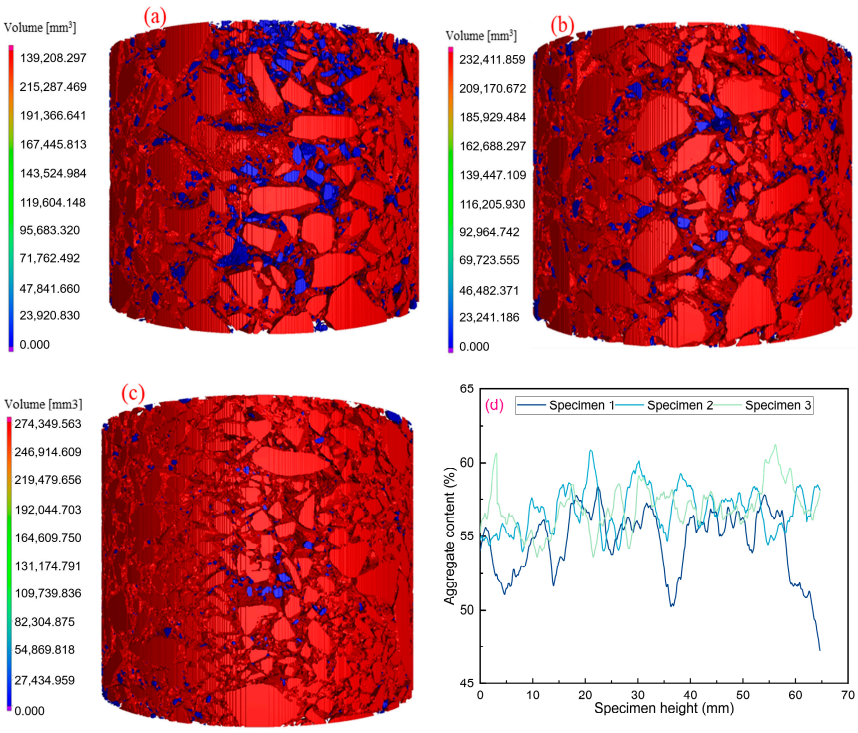


Figure 10. Aggregate distribution in mixture: (**a**) Specimen 1, (**b**) Specimen 2, (**c**) Specimen 3, and (**d**) Aggregate content.

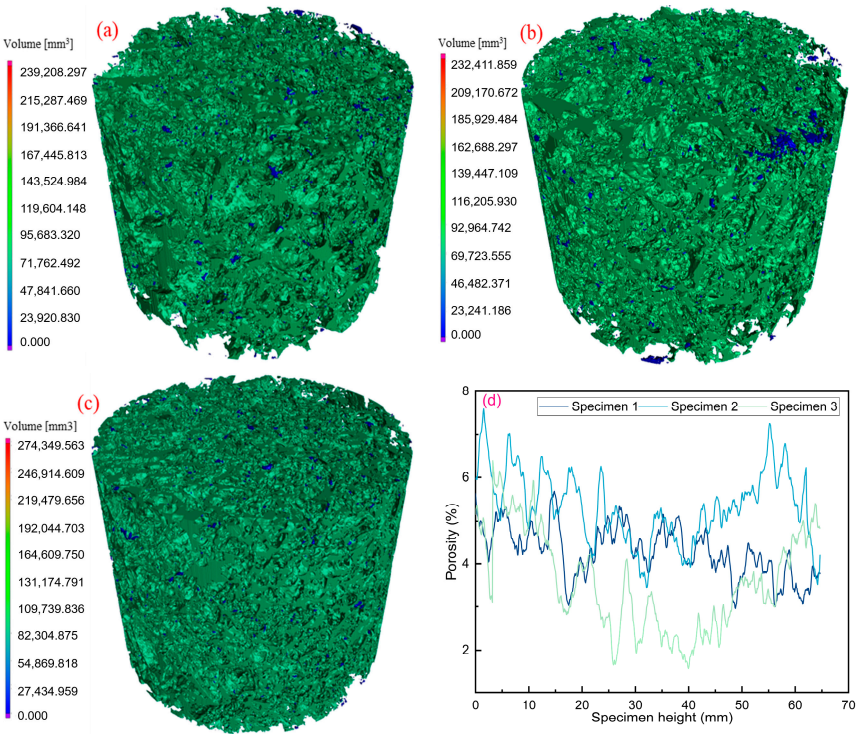


Figure 11. Porosity distribution in mixture: (**a**) Specimen 1, (**b**) Specimen 2, (**c**) Specimen 3, and (**d**) Porosity.

After three-dimensional reconstruction, voxels were segmented and classified based on grayscale contrast to distinguish the aggregate, asphalt mastic, and air-void phases [51]. Figure 9a–c shows the spatial distribution of the asphalt mortar phase in the three specimens. Overall, the mortar mainly occupied the interparticle spaces and appeared to form a

continuous matrix around the aggregate skeleton in the reconstructed images. Air voids at different scales were distributed near the specimen surface and within the interior, and they were separated from the mortar phase in the segmentation results. To quantify the vertical nonuniformity, Figure 9d presents the mortar content distribution along the specimen height. The overall trend indicates slightly lower mastic content near the end regions and relatively higher content in the middle region, while the fluctuation amplitude differed among specimens. This pattern suggests an end effect during compaction. It indicates mortar migration and redistribution along the height. The extent of this behavior may relate to end-surface conditions, differences in surface openness, and the uniformity of aggregate coating [52]. More uniform aggregate coating corresponds to a smoother variation in mortar content along the height.

After three-dimensional reconstruction, the aggregate phase was segmented based on grayscale contrast and its spatial distribution was visualized, as shown in Figure 10a–c. In the figure, the red regions represent the aggregate phase and the blue regions represent the air-void phase. The aggregates exhibited a skeleton-like spatial arrangement in the reconstructed CT images, consistent with their role as the primary load-bearing framework of the mixture. The outer boundary of the specimens appeared relatively smooth, which reflects the constraint effect of the Marshall mold during compaction. To quantify vertical nonuniformity, Figure 10d shows the aggregate content distribution along the specimen height. The three specimens had similar mean levels, but each specimen exhibited local fluctuations along the height. Overall, the aggregate content was slightly lower near the end regions and relatively higher in the middle region, while the fluctuation amplitude differed among specimens. This trend is consistent with the vertical distribution of mastic content described above. It indicates an end effect during compaction, where differences in end-surface openness and local packing structure may cause phase redistribution along the height direction. Among the three specimens, Specimen 1 showed the largest height-direction fluctuation, which suggests relatively lower uniformity of aggregate packing after compaction.

The CT-based three-dimensional reconstruction results were used to quantitatively characterize the air-void distribution, as shown in Figure 11. In the three-dimensional visualization, the green body represents the specimen and the blue phase represents the air voids. Figure 11a–c shows that the air voids appeared mainly as dispersed, small-scale features within the specimens, while a small number of relatively larger voids were observed in some local regions. Overall, the spatial distribution of air voids showed clear nonuniformity, which reflects differences in local packing structure and the degree of mastic filling at the mesoscopic scale. To evaluate vertical nonuniformity, Figure 11d presents the air-void content along the specimen height. All three specimens showed pronounced local fluctuations, and their mean levels differed across specimens. The overall trend indicates lower air-void content near the end regions and higher values in the middle region, while the magnitude of this trend varied among specimens. This feature is consistent with the end effect during Marshall compaction. Differences in constraint conditions, local packing, and mastic redistribution can cause height-direction fluctuations and nonuniform air-void distribution.

Figures 9–11 provide a description of mesostructural nonuniformity from the perspectives of the mortar, aggregate, and air-void phases. The mortar mainly occupied interparticle spaces and surrounded the aggregate skeleton in the reconstructed images. The aggregates constituted the primary load-bearing skeleton of the mixture. The air voids were mainly distributed inside the specimens in a dispersed form. Comparison of the height-direction profiles indicates that fluctuations in air-void content generally show an inverse trend to the solid-phase content. Regions with higher aggregate content or higher mortar content

usually corresponded to lower air-void content, which suggests denser local packing and more sufficient void filling. Regions with higher air-void content were often associated with looser packing or insufficient mastic filling. For all three specimens, the fluctuations were generally more pronounced near the end regions. The observed height-dependent mesostructural gradients were interpreted as compaction-related structural features associated with Marshall mold boundary effects. Overall, smoother height-dependent variations in mortar, aggregate, and air-void contents were associated with greater local mesostructural uniformity in the MT100 specimens.

4. Conclusions, Limitations, and Future Prospects

4.1. Conclusions

This study adopted an equal-volume replacement design to assess the potential of MT as an alternative mineral filler in AC-13 asphalt mixtures through pavement performance tests. Industrial CT-based three-dimensional reconstruction and phase segmentation were further applied to three specimens with 100% MT replacement. The spatial distributions of the mastic, aggregate, and air-void phases were quantitatively characterized to describe their mesostructural features and height-dependent variations. Based on the experimental results and analysis, the following conclusions were drawn.

(1) As the MT replacement ratio increased, the rutting resistance at high temperature improved. The dynamic stability increased and the accumulated rutting deformation decreased. These results indicate enhanced high-temperature deformation resistance.
(2) At 15 °C, MT replacement increased the flexural tensile strength and flexural stiffness modulus, indicating improved intermediate-temperature flexural load-bearing capacity and stiffness. The splitting tensile strength and stiffness modulus at failure also increased, while the tensile strain at failure decreased, indicating a trade-off between stiffness and deformation capacity.
(3) The immersion Marshall results showed overall increases in Marshall stability after 0.5 h and 48 h of immersion, while residual stability remained relatively high and varied only modestly among the mixtures. These findings indicate improved Marshall stability under the investigated immersion conditions.
(4) Industrial CT analysis of three specimens with 100% MT replacement characterized the spatial distributions of asphalt mortar, aggregates, and air voids, as well as their height-dependent variations. The observed vertical mesostructural nonuniformity was interpreted as a compaction-related structural feature associated with Marshall mold boundary effects.

4.2. Limitations and Prospects

This study used MT from a single source and evaluated performance mainly through wheel tracking, bending, indirect tensile splitting, and immersion Marshall tests. Long-term service conditions were not covered, such as cyclic fatigue, oxidative aging, freeze–thaw action, coupled moisture–temperature effects, and sub-zero thermal cracking. The CT analysis focused on the 100% replacement mixture as a representative case; independent validation of CT-derived air-void contents and quantitative phase-connectivity analysis were not performed. As the asphalt content was fixed at 4.8% across all replacement levels, future studies may determine mixture-specific optimum asphalt contents and volumetric properties (Va, VMA, and VFA) to evaluate effective binder film thickness. Further research may characterize filler properties and filler–binder interactions using Blaine specific surface area, Rigden void content, and contact-angle-based surface free energy analyses, while assessing source-dependent variability, long-term durability, and environmental risks. CT analysis

may also be extended to multiple replacement levels to validate and quantify mesostructural characteristics and investigate their relationships with macroscopic performance.

Supplementary Materials: The following supporting information can be downloaded at: https://www.mdpi.com/article/10.3390/buildings16214368/s1, Table S1: Descriptive statistics of asphalt mixture performance indices at different MT replacement levels; Table S2: One-way ANOVA results; Table S3: Specimen-level three-point bending test results of asphalt mixtures with different MT replacement levels.

Author Contributions: Conceptualization, J.Z. and H.G.; methodology, J.Z. and H.G.; software, J.Z.; validation, J.Z. and B.W.; formal analysis, J.Z.; investigation, J.Z., B.W., L.L., B.A., J.L. (Jinlong Liu) and J.L. (Junqi Lin); resources, J.Z., J.L. (Junqi Lin) and H.G.; data curation, B.W. and L.L.; writing—original draft preparation, J.Z.; writing—review and editing, H.G.; visualization, J.Z. and B.W.; supervision, J.L. (Junqi Lin) and H.G.; project administration, J.L. (Junqi Lin); funding acquisition, H.G. All authors have read and agreed to the published version of the manuscript.

Funding: This research was funded by the Scientific Research Fund of Institute of Engineering Mechanics, China Earthquake Administration (Grant No. 2024A01 and 2024B21); the Natural Science Foundation of Heilongjiang Province; the Fundamental Scientific Research Expenses at Heilongjiang Provincial College and University (2024-KYYWF-0076, 2022-KYYWF-1094); the Heilongjiang Province Ecological Environment Protection Research Project (HST2023GF004, HST2025GF009); and the Key Laboratory of Flood Disaster Risk Warning and Prevention and Control, Ministry of Emergency Management (2024YJ007-003).

Data Availability Statement: The data supporting the findings of this study are available from the corresponding author upon reasonable request.

Conflicts of Interest: Author Jingyuan Zhang was employed by the company Heilongjiang Provincial Transportation Planning and Design Institute Group Co., Ltd. The remaining authors declare that the research was conducted in the absence of any commercial or financial relationships that could be construed as a potential conflict of interest.

References

1. Kossoff, D.; Dubbin, W.E.; Alfredsson, M.; Edwards, S.J.; Macklin, M.G.; Hudson-Edwards, K.A. Mine Tailings Dams: Characteristics, Failure, Environmental Impacts, and Remediation. *Appl. Geochem.* **2014**, *51*, 229245. [CrossRef]
2. Franks, D.M.; Stringer, M.; Torres-Cruz, L.A.; Baker, E.; Valenta, R.; Thygesen, K.; Matthews, A.; Howchin, J.; Barrie, S. Tailings Facility Disclosures Reveal Stability Risks. *Sci. Rep.* **2021**, *11*, 5353. [CrossRef] [PubMed]
3. Hudson-Edwards, K.A.; Kemp, D.; Torres-Cruz, L.A.; Macklin, M.G.; Brewer, P.A.; Owen, J.R.; Franks, D.M.; Marquis, E.; Thomas, C.J. Tailings Storage Facilities, Failures and Disaster Risk. *Nat. Rev. Earth Environ.* **2024**, *5*, 612–630. [CrossRef]
4. Su, C.; Rana, N.M.; Zhang, S.; Wang, B. Environmental Pollution and Human Health Risk Due to Tailings Storage Facilities in China. *Sci. Total Environ.* **2024**, *928*, 172437. [CrossRef] [PubMed]
5. Abbadi, A.; Mucsi, G. A Review on Complex Utilization of Mine Tailings: Recovery of Rare Earth Elements and Residue Valorization. *J. Environ. Chem. Eng.* **2024**, *12*, 113118. [CrossRef]
6. Manaviparast, H.R.; Miranda, T.; Pereira, E.; Cristelo, N. A Comprehensive Review on Mine Tailings as a Raw Material in the Alkali Activation Process. *Appl. Sci.* **2024**, *14*, 5127. [CrossRef]
7. Adiguzel, D.; Tuylu, S.; Eker, H. Utilization of Tailings in Concrete Products: A Review. *Constr. Build. Mater.* **2022**, *360*, 129574. [CrossRef]
8. Feng, W.; Yu, Z.; Bao, R.; Xiong, J.; Yan, K.; Liu, R.; Zhang, R.; Lu, X. Manufacture of Tailings-Based Cementitious Materials: Insights into Tailings Activation Strategies. *Constr. Build. Mater.* **2024**, *439*, 137194. [CrossRef]
9. Wong, T.L.X.; Mohd Hasan, M.R.; Peng, L.C. Recent Development, Utilization, Treatment and Performance of Solid Wastes Additives in Asphaltic Concrete Worldwide: A Review. *J. Traffic Transp. Eng.* **2022**, *9*, 693–724. [CrossRef]
10. Iqbal, A.; Mashaan, N.S.; Paraskeva, T. Mining Waste in Asphalt Pavements: A Critical Review of Waste Rock and Tailings Applications. *J. Compos. Sci.* **2025**, *9*, 402. [CrossRef]
11. Li, Y.; Liu, F.; Yu, F.; Du, T. A Review of the Application of Steel Slag in Concrete. *Structures* **2024**, *63*, 106352. [CrossRef]

12. Sun, H.; Pang, L.; Ding, Y.; Xing, B.; Tang, Y.; Sun, X.; Yuan, J.; Zhou, L.; Wang, Y.; Lyu, Y.; et al. Influence of the Physical Morphological Characteristics of Mineral Fillers on the Bitumen-Filler Interfacial Interaction. *Constr. Build. Mater.* **2023**, *378*, 131206. [CrossRef]
13. Xing, B.; Du, Y.; Fang, C.; Sun, H.; Lyu, Y.; Fan, W. Particle Morphology of Mineral Filler and Its Effects on the Asphalt Binder-Filler Interfacial Interaction. *Constr. Build. Mater.* **2022**, *321*, 126292. [CrossRef]
14. Gao, H.; An, B.; Lei, X.; Gao, Y.; Liu, H. Utilization of Molybdenum Tailings as an Alternative Mineral Filler in Asphalt Mastic: Rheological Performance and Environmental Aspects. *Case Stud. Constr. Mater.* **2024**, *21*, e03639. [CrossRef]
15. Oguntayo, D.; Mashaan, N.; Shukla, S. Mine Tailings as a Sustainable Filler for Asphalt Binder–Mastics: A Review. *Materials* **2025**, *18*, 4892. [CrossRef] [PubMed]
16. Xing, B.; Fang, C.; Zhuang, C.; Lyu, Y.; Fan, W. Mineral Filler Property and Its Influence on Mastic Interfacial Cohesive Behavior at Low Temperatures. *Constr. Build. Mater.* **2023**, *364*, 129900. [CrossRef]
17. He, Y.; Zhang, J.; Gao, B.; Wang, L.; Li, Y.; Guo, F.; Huang, G. Experimental Investigation of the Interface Interaction between Asphalt Binder and Mineral Filler from the Aspects of Materials Properties. *Constr. Build. Mater.* **2023**, *393*, 132094. [CrossRef]
18. Lei, B.; Li, X.; Guo, Y.; Qu, F.; Zhao, C.; Tam, V.W.Y.; Wu, V.; Li, W. Recycling of Copper Tailing as Filler Material in Asphalt Paving Mastic: A Sustainable Solution for Mining Waste Recovery. *Case Stud. Constr. Mater.* **2024**, *20*, e03237. [CrossRef]
19. Calandra, P.; Quaranta, S.; Apolo Miranda Figueira, B.; Caputo, P.; Porto, M.; Oliviero Rossi, C. Mining Wastes to Improve Bitumen Performances: An Example of Circular Economy. *J. Colloid Interface Sci.* **2022**, *614*, 277–287. [CrossRef] [PubMed]
20. Shaikh, S.; Tiwari, A.; Gupta, A. Understanding the Influence of Design Factors and Volumetrics on Moisture Susceptibility of Hot-Mix Asphalt. *J. Mater. Civ. Eng.* **2024**, *36*, 04024228. [CrossRef]
21. Hu, J.; Chen, Y.; Chen, M.; Yu, Y.; Song, S.; Wu, J.; Qin, X. Research on the Moisture Stability of Asphalt Mixtures with Three Solid Waste Fillers. *Materials* **2023**, *16*, 7261. [CrossRef] [PubMed]
22. Adwar, N.N.; Albayati, A.H. Enhancing Moisture Damage Resistance in Asphalt Concrete: The Role of Mix Variables, Hydrated Lime and Nanomaterials. *Infrastructures* **2024**, *9*, 173. [CrossRef]
23. Liu, L.; Huang, W.; Liu, L.; Ye, F.; Chen, S.; Yang, R. Moisture Susceptibility Evaluation of Asphalt Mixture with Account of Horizontal Loads: A Novel Test Method. *Constr. Build. Mater.* **2024**, *417*, 135301. [CrossRef]
24. Jwaida, Z.; Al Quraishy, Q.A.; Almuhanna, R.R.A.; Dulaimi, A.; Bernardo, L.F.A.; Andrade, J.M.D.A. The Use of Waste Fillers in Asphalt Mixtures: A Comprehensive Review. *CivilEng* **2024**, *5*, 801–826. [CrossRef]
25. Xu, X.; Yuan, L.; Cong, P.; Wang, Z.; Zhou, X.; Wang, J.; Liu, J. Self-Healing Microcapsule Properties Improvement Technology: Key Challenges and Solutions for Application in Asphalt Materials. *Constr. Build. Mater.* **2024**, *439*, 137298. [CrossRef]
26. Ma, X.; Zhang, C.; Li, R.; Zheng, L.; Xu, J. Effect of Temperature and Humidity Environment on the Microstructure and Physicochemical Properties of SBS Modified Asphalt. *Case Stud. Constr. Mater.* **2025**, *22*, e04192. [CrossRef]
27. Liu, G.; Huang, T.; Lyu, L.; Liu, Z.; Ma, C. Effective Load Transfer Capacity Analysis for Asphalt Mixture Skeleton Based on Main Force Chain Characteristics and Discrete Element Method. *J. Mater. Civ. Eng.* **2023**, *35*, 04023303. [CrossRef]
28. Liu, G.; Han, D.; Jia, Y.; Zhao, Y. Asphalt Mixture Skeleton Main Force Chains Composition Criteria and Characteristics Evaluation Based on Discrete Element Methods. *Constr. Build. Mater.* **2022**, *323*, 126313. [CrossRef]
29. Shi, C.; Qian, G.; Yu, H.; Zhu, X.; Yuan, M.; Dai, W.; Ge, J.; Zheng, X. Research on the Evolution of Aggregate Skeleton Characteristics of Asphalt Mixture under Uniaxial Compression Loading. *Constr. Build. Mater.* **2024**, *413*, 134769. [CrossRef]
30. Sheidaei, M.; Östlund, J.-A.; Antunes, V.; Freire, A.C. Effect of the Geometrical and Physical Nature of Filler on the Rheological Properties of Mastics. *Int. J. Pavement Eng.* **2025**, *26*, 2582712. [CrossRef]
31. Wang, S.; Wang, Z.; Yu, A.; Yu, H.; He, Z.; Meng, X.; Gong, Z.; Guan, D.; Zhang, F. Characterizing the Interaction Between Asphalt and Mineral Fillers in Hot Mix Asphalt Mixtures: A Micromechanical Approach. *Appl. Sci.* **2025**, *15*, 2735. [CrossRef]
32. Jia, Y.; Yang, Y.; Zhou, T.; Gao, Y.; Wang, S.; Wei, Z. Stiffening Effect of Filler on Asphalt Mastic Composite: A New Insight Based on Nearest Surface Function. *Constr. Build. Mater.* **2022**, *344*, 128177. [CrossRef]
33. Mukhtar, N.; Mohd Hasan, M.R.; Mohd Ghazali, M.F.H.; Mohd Zin, Z.; Shariff, K.A.; Sani, A. Influence of Concentration and Packing of Filler Particles on the Stiffening Effect and Shearing Behaviour of Asphalt Mastic. *Constr. Build. Mater.* **2021**, *295*, 123660. [CrossRef]
34. Dong, J.; Zhang, K.; Liang, S.; Ma, H.; Huang, T.; Luo, R. Evaluation of Moisture Sensitivity of Asphalt Mixtures Based on Surface Energy of Asphalt Mastic. *J. Mater. Civ. Eng.* **2024**, *36*, 04024191. [CrossRef]
35. E, G.; Zhang, J.; Shen, Q.; Ji, P.; Wang, J.; Xiao, Y. Influence of Filler Type and Rheological Properties of Asphalt Mastic on the Asphalt Mastic–Aggregate Interaction. *Materials* **2023**, *16*, 574. [CrossRef] [PubMed]
36. Xu, O.; Xiang, S.; Yang, X.; Liu, Y. Estimation of the Surface Free Energy and Moisture Susceptibility of Asphalt Mastic and Aggregate System Containing Salt Storage Additive. *Constr. Build. Mater.* **2022**, *318*, 125814. [CrossRef]
37. Wang, F.; Xiao, Y.; Chen, Z.; Cui, P.; Liu, J.; Wang, N. Morphological Characteristics of Mineral Filler and Their Influence on Active Adhesion between Aggregates and Bitumen. *Constr. Build. Mater.* **2022**, *323*, 126520. [CrossRef]

38. Chen, Y.; Xu, S.; Tebaldi, G.; Romeo, E. Role of Mineral Filler in Asphalt Mixture. *Road Mater. Pavement Des.* **2022**, *23*, 247–286. [CrossRef]
39. Ling, M.; Ji, J.; Tanvir, H.; Fuentes, L.; Walubita, L.F. Simultaneous Evaluation of Rutting-Stripping Performance and Cracking Resistance for Asphalt Mixtures. *Constr. Build. Mater.* **2023**, *408*, 133581. [CrossRef]
40. Gong, X.; Jiang, Y.; Ou, S.; Qian, G.; Liu, Z. Characterization on the Mesostructural Distribution of Asphalt Mixtures via Digital Image Processing and Relation to Macroscopic Performances. *Constr. Build. Mater.* **2023**, *404*, 133212. [CrossRef]
41. Rahaman, M.Z.; Bahia, H.U. Effects of Filler Properties on Fatigue Performance and Bond Strength of Asphalt Mastics. *J. Mater. Civ. Eng.* **2023**, *35*, 04022408. [CrossRef]
42. Zhao, W.; Yang, Q. Study on the Applicability of Asphalt Concrete Skeleton in the Semi-Flexible Pavement. *Constr. Build. Mater.* **2022**, *327*, 126923. [CrossRef]
43. Yin, P.; Pan, B.; Liu, Y. Effect of Different Filler Substitution Ratios on the Service Performance of Asphalt Mixtures: Using Coal-Based Synthetic Natural Gas Slag as Substitute Filler. *Constr. Build. Mater.* **2024**, *456*, 139245. [CrossRef]
44. Chen, Z.; Leng, Z.; Jiao, Y.; Xu, F.; Lin, J.; Wang, H.; Cai, J.; Zhu, L.; Zhang, Y.; Feng, N.; et al. Innovative Use of Industrially Produced Steel Slag Powders in Asphalt Mixture to Replace Mineral Fillers. *J. Clean. Prod.* **2022**, *344*, 131124. [CrossRef]
45. *JTG E20-2011*; Standard Test Methods of Bitumen and Bituminous Mixtures for Highway Engineering. China Communications Press: Beijing, China, 2011.
46. Wei, Z.; Jia, Y.; Wang, S.; Li, Z.; Li, Y.; Wang, X.; Gao, Y. Utilization of Iron Ore Tailing as an Alternative Mineral Filler in Asphalt Mastic: High-Temperature Performance and Environmental Aspects. *J. Clean. Prod.* **2022**, *335*, 130318. [CrossRef]
47. Pan, Y.; Guo, H.; Guan, W.; Zhao, Y. A Laboratory Evaluation of Factors Affecting Rutting Resistance of Asphalt Mixtures Using Wheel Tracking Test. *Case Stud. Constr. Mater.* **2023**, *18*, e02148. [CrossRef]
48. Ou, L.; Zhu, H.; Chen, R.; Su, C.; Yang, X. Effect of Industrial Solid Waste as Fillers on the Rheology and Surface Free Energy of Asphalt Mastic. *Materials* **2024**, *17*, 1125. [CrossRef] [PubMed]
49. Wang, R.; Zhao, Y. Influence of Water Molecule Distribution on Asphalt-Aggregate Interface Debonding: Insights from Adhesion Energy and Hydrogen Bonding. *Colloids Surf. A Physicochem. Eng. Asp.* **2025**, *719*, 137034. [CrossRef]
50. Chen, B.; Wang, R.; Yu, X.; Dong, F.; Ding, G. Identifying the Influence of Asphalt Mixture Workability Improvement on the Characteristics of Asphalt, Aggregate and Void after Compaction Utilising CT Scanning Technology. *Constr. Build. Mater.* **2024**, *448*, 138172. [CrossRef]
51. Shan, L.; Yang, H.; Guo, F.; Li, Z. Fatigue Damage Evolution in Asphalt Mixture Based on X-Ray CT Images. *Constr. Build. Mater.* **2022**, *358*, 129242. [CrossRef]
52. Gong, X.; Ma, J.; Qian, G.; Yu, H.; Zhong, C. Determination and Quantitative Representation of Three-Level Dispersion System in Asphalt Mixture Interface Area. *Mater. Des.* **2025**, *253*, 113879. [CrossRef]

Disclaimer/Publisher's Note: The statements, opinions and data contained in all publications are solely those of the individual author(s) and contributor(s) and not of MDPI and/or the editor(s). MDPI and/or the editor(s) disclaim responsibility for any injury to people or property resulting from any ideas, methods, instructions or products referred to in the content.